Investigation of the High-energy Emission from the Magnetar-like Pulsar PSR J1119–6127 after the 2016 Outburst

Lupin Chun-Che Lin[1] , Hui-Hui Wang[2], Kwan-Lok Li[3], Jumpei Takata[2] , Chin-Ping Hu[4] , C.-Y. Ng[4] , C. Y. Hui[5] ,
A. K. H. Kong[6] , Pak-Hin T. Tam[7] , and Paul K. H. Yeung[8]
[1] Department of Physics, UNIST, Ulsan 44919, Republic of Korea; lupin@unist.ac.kr
[2] School of Physics, Huazhong University of Science and Technology, Wuhan 430074, People's Republic of China
[3] Department of Physics and Astronomy, Michigan State University, East Lansing, MI 48824, USA
[4] Department of Physics, The University of Hong Kong, Pokfulam Road, Hong Kong
[5] Department of Astronomy and Space Science, Chungnam National University, Daejeon 305-764, Republic of Korea
[6] Institute of Astronomy, National Tsing Hua University, Hsinchu, Taiwan
[7] School of Physics and Astronomy, Sun Yat-Sen University, Zhuhai 519082, People's Republic of China
[8] Institute of Experimental Physics, Department of Physics, University of Hamburg, Luruper Chaussee 149, D-22761 Hamburg, Germany

Abstract

PSR J1119−6127 is a radio pulsar that behaved with magnetar-like bursts, and we performed a comprehensive investigation of this pulsar using the archival high-energy observations obtained after its outburst in 2016 July. After the 2016 outburst, specific regions on the neutron star (NS) surface were heated up to >0.3 and >1 keV from $\sim$0.2 keV. A hard nonthermal spectral component with a photon index <0.5 related to the magnetospheric emission can be resolved from the *NuSTAR* spectra above 10 keV. We find that the thermal emitting regions did not cool down and gradually shrank by about 20%–35% 4 months after the outburst. Hard X-ray pulsations were detected with *NuSTAR* immediately after the outburst at a 5σ confidence level and with a background-subtracted pulsed fraction of 40% ± 10%. However, the signal became undetectable after a few days. Using *Fermi* data, we found that the gamma-ray emission in 0.5–300 GeV was suppressed along with the disappearance of the radio pulsations. This is likely caused by a reconfiguration of the magnetic field. We also discovered that the timing noise evolved dramatically, and the spin-down rate significantly increased after the 2016 glitch. We proposed that postoutburst temporal and spectral behaviors from radio to gamma-ray bands were caused by changes of the magnetosphere structure, pair plasma injection, and the shrinking emission sites on the NS.

Key words: gamma rays: stars – magnetic fields – methods: data analysis – pulsars: individual (PSR J1119-6127) – X-rays: bursts

1. Introduction

Magnetars are a special class of pulsars that have relatively long spin periods and extremely strong surface magnetic fields of 10^{14}–10^{15} G (Kaspi & Beloborodov 2017), although some of them can have relatively weak surface fields (e.g., $\sim6 \times 10^{12}$ G for SGR 0418+5729; Rea et al. 2013). The soft X-ray emission of magnetars is commonly believed to be powered by the decay of the magnetic field (Thompson & Duncan 1996). One of the most intriguing features of magnetars is bursts in hard X-rays/soft γ-rays (Woods & Thompson 2006; Ng et al. 2011; Pons & Rea 2012) when the local magnetic stress becomes too strong to be balanced by the restoring force of the crust or the reconnection of the magnetic field leads to a change of the magnetosphere structure. Some rotation-powered pulsars (RPPs) with a high surface magnetic field strength ($\gtrsim 4 \times 10^{13}$ G; hereafter high-B pulsars) show similar outburst activities and are now considered as the transitional objects between canonical RPPs and magnetars (Kaspi & McLaughlin 2005; Ng & Kaspi 2011; Hu et al. 2017). High-B pulsars and magnetars also share similar features in their outburst activities, glitch sizes, and inferred level of timing noise. Studies of high-B pulsars are essential to unify the connection between magnetars and isolated neutron stars (NSs)/radio pulsars (Pons & Geppert 2007; Perna & Pons 2011; Viganò et al. 2013). Most high-B pulsars were detected in the radio band (e.g., PSRs J1718−3718, J1814−1733, and J1814−1733; Camilo et al. 2000; McLaughlin et al. 2003; Hobbs et al. 2004) and a few of

them are radio-quiet (e.g., PSR J1846−0258; Archibald et al. 2008; Gavriil et al. 2008). Similar to some transient magnetars (e.g., 1E 1547.0−5408; Burgay et al. 2009), intermittent and variable radio pulses were detected from some high-B pulsars (Thompson 2008). Among this class of objects, PSR J1119−6127 is a particularly interesting case because it has a confirmed rotational period of $\sim$408 ms detected in the radio (Camilo et al. 2000), X-ray (Gonzalez et al. 2005), and γ-ray (Parent et al. 2011) bands, which permits a rich, multiwavelength investigation.

PSR J1119−6127 is associated with the supernova remnant (SNR) G292.2−0.5 (Pivovaroff et al. 2001; Ng et al. 2012), and its pulsar wind nebula (PWN) was resolved by *Chandra* (Gonzalez & Safi-Harb 2003). Based on the measurements through H I absorption, the distance of the pulsar is inferred to be 8.4 kpc (Caswell et al. 2004). According to the detected spin-down rate $\dot{P} = 4.0 \times 10^{-12}$ (Camilo et al. 2000), the inferred surface magnetic field is 4.1×10^{13} G, and the spin-down luminosity is $\dot{E} = 2.3 \times 10^{36}$ erg s^{-1}. The characteristic age was estimated as 1600 yr, with the breaking index 2.684 ± 0.002 determined from radio timing data over 12 yr (Weltevrede et al. 2011). PSR J1119−6127 experienced three glitches in 1999, 2004, and 2007 (Camilo et al. 2000; Weltevrede et al. 2011; Antonopoulou et al. 2015), but no outburst event was detected before. Recoveries were observed following all these glitches (Weltevrede et al. 2011), similar to that of many pulsars and magnetars (Dib et al. 2008).

The Gamma-ray Burst Monitor on board the *Fermi Gamma-ray Space Telescope* was triggered by a magnetar-like burst of PSR J1119−6127 on 2016 July 27 (Younes et al. 2016), and the *Neil Gehrels Swift Observatory* (hereafter *Swift*) Burst Alert Telescope also reported a similar burst after a few hours (Kennea et al. 2016). The known X-ray pulsations were subsequently confirmed by the X-Ray Telescope (XRT) on board *Swift* (Antonopoulou et al. 2016), and several investigations were performed to study its timing and spectral behavior in the postoutburst stage (Archibald et al. 2016b; Majid et al. 2016). Based on the detailed examination with an S/N-based search and a Bayesian blocks algorithm, 13 short X-ray bursts were identified between 2016 July 26 and 28 (Göğüş et al. 2016). The pulsar showed a spin-up glitch of $\Delta \nu = 1.40(2) \times 10^{-5}$ Hz and $\Delta \dot{\nu} = -1.9(5) \times 10^{-12}$ Hz s^{-1} soon after the onset of the 2016 outburst (Archibald et al. 2016a; hereafter after the 2016 outburst). The initial follow-up radio observations did not detect any pulsations, but the signal reemerged over a large frequency band with different pulse profiles in 2016 mid-August (Majid et al. 2017). Such a transient radio emission feature could be associated with the glitching activity, as seen from magnetars (Camilo et al. 2006). In addition, there was a significant difference in the radio pulse profile shape before and after the outburst, from single-peaked to a complex profile with multiple components at 1.4 GHz (Archibald et al. 2017). All of the observed features, including the outburst behavior and the unusual change of the radio profiles, are similar to those of transient magnetars.

The X-ray spectrum of PSR J1119−6127 consists of thermal and nonthermal components in the quiescent state (Gonzalez et al. 2005; Safi-Harb & Kumar 2008; Ng et al. 2012). The thermal emission can be attributed to a hotspot with $kT \sim 0.21$ keV or NS atmospheric emission with $kT = 0.06-0.17$ keV, and the nonthermal component can be described by a simple power law (PL) with a photon index (Γ) of 1.6–2.1. The γ-ray spectrum can be characterized with a PL with an exponential cutoff (PLEC), similar to other RPPs (Parent et al. 2011). After the 2016 outburst, the X-ray spectrum was dominated by a thermal component, and the PL component became harder with a photon index of 1.2 ± 0.2, extending to the hard X-ray band (Archibald et al. 2016a). The 0.5–10 keV luminosity is 3.5×10^{35} erg s^{-1}, corresponding to $\sim 15\%$ of the pulsar spin-down power and comparable to the preoutburst γ-ray (>0.1 GeV) luminosity (Parent et al. 2011). At the end of 2016 October, a single PL with a softer photon index of 2.0 ± 0.2 was sufficient to model the X-ray spectrum (Blumer et al. 2017).

In this paper, we analyze the publicly available high-energy observations taken after the outburst. The observations are described in Section 2. We search for spin periodicities via data counting statistics at different epochs. Then we trace the spin period evolution with phase-coherent analysis. We obtain the X- and γ-ray spectra before and after the outburst and perform a quantitative comparison. The results are presented in Section 3. Based on our results, we present a coherent picture and discuss emission scenarios in Section 4. A global magnetosphere reconfiguration could serve as the most possible origin. Our contribution and two recently published articles including the long-term investigations of PSR J1119−6127 in the radio (Dai et al. 2018) and X-ray bands (Archibald et al. 2018) can certainly provide a better understanding of the outburst/glitch event that occurred in this pulsar and further clarify its connection to transient radio RPPs and magnetars.

2. High-energy Observations

In order to characterize the high-energy emission of PSR J1119−6127, we analyzed the archival data obtained from the *Swift*, *XMM-Newton*, *Nuclear Spectroscopic Telescope Array* (*NuSTAR*), and *Fermi* observatories. The pulsar position at R.A. = $11^{\rm h}19^{\rm m}14.^{\rm s}26$, decl. = $-61°27'49.''3$ (J2000) was obtained from *Chandra* (Safi-Harb & Kumar 2008; Blumer et al. 2017) to perform the timing analysis of X-ray observations. All the photon arrival times were corrected to the barycentric dynamical time (TDB) with the JPL DE200 solar system ephemeris at the source position determined by *Chandra* (Safi-Harb & Kumar 2008) for all data sets.

2.1. Fermi

We obtained the *Fermi* Large Area Telescope (LAT) Pass 8 (P8R2) data in the energy range of 0.5–300 GeV. This range was chosen to minimize contamination by other sources in the source-crowded region (Parent et al. 2011). We considered the LAT data collected within 2013 November (MJD ∼ 56,600)–2016 December (MJD ∼ 57,750). Photons in a circular region of interest (ROI) within 20° and 1° from the position of 3FGL J1119.1−6127, corresponding to PSR J1119−6127, determined in the LAT 4 yr point-source catalog (Acero et al. 2015) are taken into account for spectral and temporal analysis, respectively. The data reduction was processed with *Fermi* Science Tools (v10r0p5).

We selected events in the class for the point source or Galactic diffuse analysis (i.e., event class 128) and considered photons collected in the front and back sections of the tracker (i.e., evttype = 3). We used the instrument response function "P8R2_SOURCE_V6" throughout this study. We also excluded events with zenith angles larger than 90° to reduce contamination from Earth's albedo γ-rays, and the data quality is constrained by the good time interval of the spacecraft (i.e., DATA_QUAL > 0). In the timing analysis, all photon arrival times were corrected to TDB with the task *gtbary* supported under *Fermi* Science Tools.

2.2. Swift

We considered all of the XRT observations operated under the windowed timing (WT) mode to perform the timing analysis, since only this mode provides a high enough time resolution of 1.76 ms. All data were obtained from the HEASARC[9] archive, and we obtained the light curves and spectra using the XRTGRBLC task in the HEASOFT package (v.6.22). We extracted the source counts from a box region of $15'' \times 35''$, which is the default setting of the XRTGRBLC task. Only photon energies in the range of 0.3–10 keV with grades 0–2 were included for further analysis. We corrected the photon arrival times to TDB using the HEASOFT task *barycorr*.

2.3. XMM-Newton

After the outburst, *XMM-Newton* observed PSR J1119−6127 on 2016 August 6, 15, and 30 and December 13 with

---

exposure of ∼21.6, 29.5, 34, and 49 ks, respectively. All EPIC cameras were operated in the small-window mode with the thin filter. We considered single- to quadruple-pixel events (PATTERN = 0–12) for MOS (Metal Oxide Semi-conductor) and single and double events (PATTERN = 0–4) for pn (camera). All data reduction was performed using the latest *XMM-Newton* Science Analysis Software (XMMSAS; version 16.1.0). We also filtered out artifacts from the calibrated and concatenated data set and put the most conservative event-screening criteria as "FLAG==0." We removed all the photons collected in short bursts (e.g., Archibald et al. 2017) and time intervals contaminated by X-ray background flares in both timing and spectral analyses. We extracted events in 0.15–12 keV from a 20″ radius region centered on the *Chandra* position. Note that this radius encircles ∼76% of the energy. We corrected the photon arrival times to TDB using the XMMSAS task *barycen* for the following timing analysis. In the spectral analysis, we determined the background in the nearby source-free region and generated the response matrices and ancillary response files with the XMMSAS tasks *rmfgen* and *arfgen*.

2.4. NuSTAR

Nonthermal X-rays related to PSR J1119−6127 can have higher energy after bursts, so we also included the *NuSTAR* observations, which have an effective energy range of 3–79 keV (Harrison et al. 2013). *NuSTAR* started to observe PSR J1119−6127 following the main magnetar-like outburst on 2016 July 28. Each datum of *NuSTAR* was observed with the onboard Focal Plane Modules A and B (FPMA/B). Excluding two slew observations and some with exposures less than 1 ks, we have five observations from 2016 July 28; August 5, 14, and 30; and December 12, corresponding to exposures of ∼54.4, 87.2, 95.4, 92.1, and 94.3 ks, respectively. We carried out a detailed temporal and spectral analysis on the latter four data sets, which were jointly observed with *XMM-Newton*. We only performed the temporal analysis on the first data set (ObsID 80102048002), since the joint spectral fit with the *Swift* observation has previously been reported (Archibald et al. 2016a).

We also used the HEASOFT package (v.6.22) together with NuSTARDAS v1.8.0 and the updated *NuSTAR* calibration database (CALDB version 20171204) for the data analysis. We adopted a source region of 60″ radius (and 30″ for the last observation, during which the source was faint) and a source-free background region with a radius of 90″. We extracted events with a pulse-invariant channel of 35–1909, which corresponds to the default energy range of 3–79 keV, and generated the response matrices using the *nuproducts* tasks. Similar to the *Swift* data, we also used the *barycorr* task to perform the barycentric time correction.

3. Results

We analyzed the X-ray and γ-ray data of PSR J1119−6127 mentioned in Section 2 and inspected the spin periodicity and spectral behavior of our target at different epochs. In the following subsections, we will present the detailed procedures in our analyses and the complete results.

3.1. X-Ray Timing Analysis

We only utilized the data obtained with the PN camera for *XMM-Newton* observations to perform timing analysis because of its sufficient temporal resolution (5.7 ms). We extrapolated the preoutburst timing solution to search for the periodic signals among all the X-ray data. We performed 100 trials with a step size determined by the Fourier width (i.e., 1/time span of the data). Only spin frequencies with a chance probability of the signal less than 5.7×10^{-7} (i.e., 5σ confidence level) yielded from *H*-statistics (de Jager & Büsching 2010) are presented in Table 1. Because the pulse profiles are mostly single-peaked, all the results also correspond to a significant Rayleigh power (Mardia 1972; Gibson et al. 1982), except for ObsID 00034632002 investigated by *Swift*. The evolution of the spin frequency detected in X-ray data is shown in Figure 1, and the spin-down rate drastically increased after the end of 2016 July.

Figure 2 shows the folded light curves in the different energy bands. In the soft (0.15 or 0.3–2.5 keV) and medium (3–10 keV) X-ray bands, there is no significant structural change with aligned pulsed peaks in the pulse profile, consistent with that reported by Archibald et al. (2016a). In the hard X-ray band (10–79 keV), we found a double-peaked pulse profile on July 28–29 with a false-alert probability of 7.7×10^{-7} through *H*-statistics. Nevertheless, the hard X-ray pulsations became much weaker after August and were only detected at less than a 3σ level.

We traced the times of arrival (TOAs; Ray et al. 2011) inferred from the positive detections mentioned in Table 1 using a maximum-likelihood method (Livingstone et al. 2009) to account for the influence of timing noise. Because the X-ray instruments cover different effective energy ranges, we folded the data covering the similar observational time with the same ephemeris and examined the structure change of the pulse profiles. Figure 3 shows examples of the comparison between the profiles obtained from different instruments. There is no obvious phase lag of the major peak determined in soft and hard X-rays; we therefore included all the X-ray data in the TOA analysis. Each TOA was determined with enough, say, >300, counts to resolve the position of the main peak in the pulse profile. To avoid the unbalanced weighting caused by lots of TOAs determined from *XMM* and *NuSTAR* over a short time interval, we determined one TOA with a duration of ∼5–8 ks for the *XMM* data and ∼18–20 ks for the *Swift* and *NuSTAR* observations.

From MJD ∼ 57,598 to MJD 57,616, two high-order polynomial terms ($\ddot{\nu}$ and $\dddot{\nu}$) are required to describe the timing noise, and the result is shown in Table 2. We note that the derived spin frequency and the spin-down rate are consistent with those determined by Archibald et al. (2016a). If we extend the effective time range of the pulsar ephemeris for more than half a month, the modified solution can be referred to the lower panel of Table 2, and the timing residuals are displayed in Figure 4. We found that more high-order terms are needed, and such a feature can also be applied to characterize the change of the spin-down rate in different time intervals, as shown in Figure 1. Since the next positive detection after MJD ∼ 57,630 is 1 month later and the uncertainties in the timing solution are large, these will lead to cycle count ambiguity in the following TOA analysis, and we cannot further extend the ephemeris of PSR J1119−6127.

3.2. γ-Ray Light Curve and Spectrum

We performed unbinned-likelihood analysis using the "NewMinunit" optimization algorithm to derive the flux of

Table 1
Spin Period of PSR J1119−6127 Determined from the X-Ray Data after the 2016 Outburst

Start Obs. Date	Instruments	Duration (ks)	ObsID	Photons	Epoch Zero[a] (MJD)	Spin Frequency[b] (Hz)	Z_1^2/H	Chance Prob.
2016 Jul 28[c]	*Swift*/XRT	35.4	00034632001	3846	57,598.0	2.439842(1)	503/571	$<10^{-11}$
2016 Jul 28[c]	*NuSTAR*/FPM	82.9	80102048002	32,265	57,598.5	2.4398409(2)	5820/6980	$<10^{-11}$
2016 Jul 31[c]	*Swift*/XRT	17.9	00034632002	424	57,600.2	2.43983(2)	28.6/47.6	5.4×10^{-7}
2016 Aug 05	*NuSTAR*/FPM	127.0	80102048004	40,275	57,606.0	2.4398219(1)	7670/9310	$<10^{-11}$
2016 Aug 06	*XMM*/PN	20.1	0741732601	25,530	57,606.6	2.4398214(8)	7070/7990	$<10^{-11}$
2016 Aug 09	*Swift*/XRT	57.6	00034632007	1376	57,609.5	2.43814(2)	151/177	$<10^{-11}$
2016 Aug 10	*Swift*/XRT	5.9	00034632008	339	57,610.25	2.43979(3)	64.5/79.9	$<10^{-11}$
2016 Aug 14	*NuSTAR*/FPM	170.8	80102048006	32,473	57,615.0	2.4397973(1)	5340/6320	$<10^{-11}$
2016 Aug 15	*XMM*/PN	27.9	0741732701	26,060	57,616.0	2.4397945(6)	7020/7850	$<10^{-11}$
2016 Aug 26	*Swift*/XRT	70.5	00034632010	627	57,627.0	2.439746(3)	49.4/54.1	4.0×10^{-8}
2016 Aug 30	*XMM*/PN	32.5	0741732801	19,466	57,630.3	2.4397218(6)	4960/5540	$<10^{-11}$
2016 Aug 30	*Swift*/XRT	17.9	00034632011	542	57,630.4	2.439720(8)	78.1/105	$<10^{-11}$
2016 Aug 30	*NuSTAR*/FPM	166.5	80102048008	20,878	57,631.0	2.4397154(2)	1810/1880	$<10^{-11}$
2016 Sep 27	*Swift*/XRT	6.4	00034632020	527	57,658.05	2.43964(2)	72.7/99.9	$<10^{-11}$
2016 Dec 12	*NuSTAR*/FPM	183.3	80102048010	2118	57,735.0	2.4391775(8)	175/203	$<10^{-11}$
2016 Dec 13	*XMM*/PN	47.5	0762032801	4053	57,735.5	2.439177(1)	954/1020	$<10^{-11}$

Notes.
[a] The time zero determined in the periodicity search.
[b] The uncertainties quoted in parentheses were assessed by Equation 6(a) in Leahy (1987).
[c] Data sets also used by Archibald et al. (2016a) to generate the timing ephemeris.
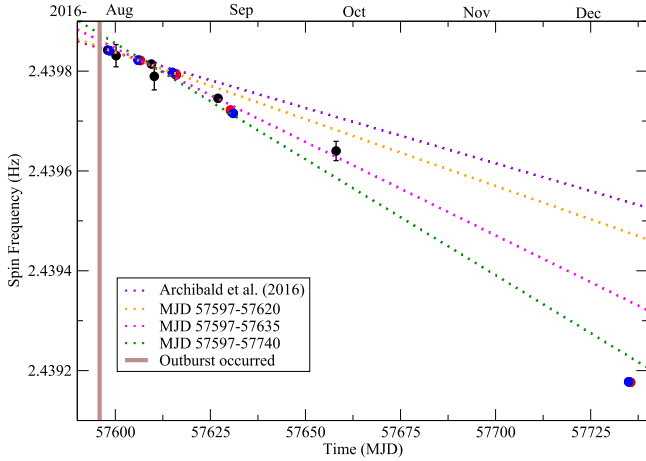
Figure 1. Evolution of the frequency of PSR J1119−6127 determined from the archival X-ray data after the 2016 magnetar-like outburst. The black, red, and blue data points represent the best-fit frequency obtained from *Swift*/XRT, *XMM*/PN, and *NuSTAR*/FPM, respectively. The brown solid line labels the onset of the 2016 outburst. The dotted lines denote the linear regression over different time intervals. The magenta dotted lines describe the postoutburst ephemeris reported by Archibald et al. (2016a) with a spin frequency (ν) = 2.43983734(8) s^{-1} and spin-down rate ($\dot{\nu}$) = $-2.57(5) \times 10^{-11}$ s^{-2} at the epoch of MJD 57,600. At the same epoch zero, orange, pink, and green lines correspond to $\dot{\nu}$ of $-3.10(3) \times 10^{-11}$, $-4.3(3) \times 10^{-11}$, and $-5.4(2) \times 10^{-11}$ s^{-2}, respectively.

our target. Spectral parameters of other sources in the ROI are based on the LAT 4 yr point-source (3FGL; Acero et al. 2015) catalog, and the standard templates of Galactic and isotropic background (gll_iem_v06.fits and iso_P8R2_SOURCE_V6. txt) are also included in our analysis. The spectral parameters of each source including PSR J1119−6127 in ROI are thawed, and we assume the PLEC model for our target. We divided the data into 60 day bins to investigate the variation of the source flux. This result is shown in Figure 5. Between MJD 57,570 and 57,630, the pulsar experienced a magnetar-like outburst,
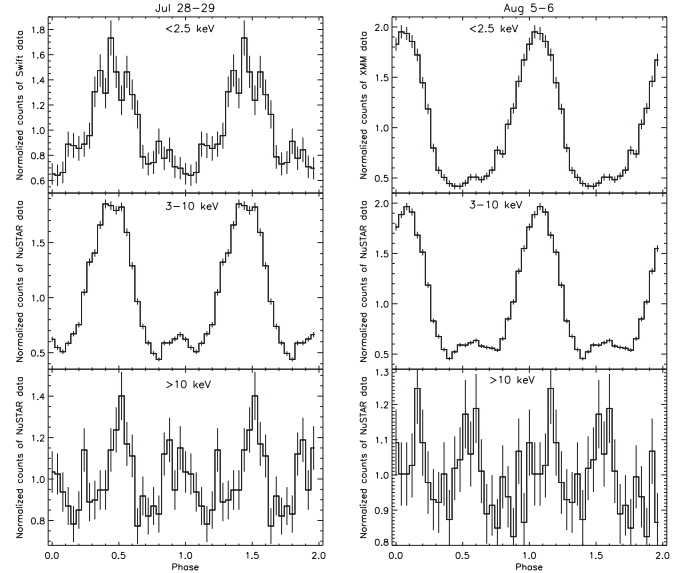
Figure 2. Postoutburst X-ray pulse profiles of PSR J1119-6127 taken on July 28–29 (left panels) and August 5–6 (right panels). The soft X-ray band profiles are obtained from *Swift*/XRT and *XMM*/PN, respectively, and the medium and hard X-ray profiles are from *NuSTAR*/FPM. Two cycles of each profile are shown for clarity.
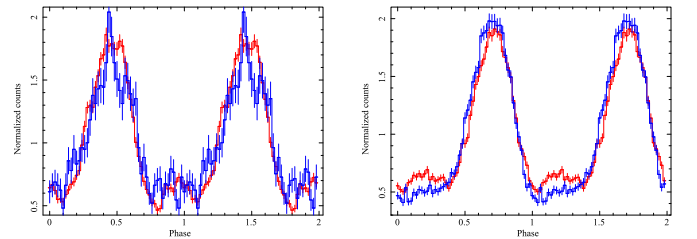

Figure 3. Comparison of the pulse profiles obtained from the different instruments. The left panel shows *Swift*/XRT (blue line) vs. *NuSTAR*/FPM (red line), and the right panel shows *XMM*/PN (blue line) vs. *NuSTAR*/FPM (red line). Two cycles of each profile are shown for clarity.

Table 2
Local Ephemeris of PSR J1119−6127 Derived with TOA Analysis
through X-Ray Data in Table 1

Parameter	
Pulsar name	PSR J1119−6127
Valid MJD range	57,598–57,616
R.A., α	11:19:14.26[a]
Decl., δ	−61:27:49.3[a]
Pulse frequency, ν (s^{-1})	2.4398374(1)
First derivative of pulse frequency, $\dot{\nu}$ (s^{-2})	−2.58(4) × 10^{-11}
Second derivative of pulse frequency, $\ddot{\nu}$ (s^{-3})	−9(10) × 10^{-19}
Third derivative of pulse frequency, $\dddot{\nu}$ (s^{-4})	−1.3(1) × 10^{-23}
Epoch of frequency determination (MJD)	57,600
Time system	TDB
rms timing residual (ms)	3.5
χ^2_ν/dof	1.30/34
Valid MJD range	57,598–57,632
Pulse frequency, ν (s^{-1})	2.4398376(2)
First derivative of pulse frequency, $\dot{\nu}$ (s^{-2})	−2.5(2) × 10^{-11}
Second derivative of pulse frequency, $\ddot{\nu}$ (s^{-3})	−1.5(8) × 10^{-18}
Third derivative of pulse frequency, $\dddot{\nu}$ (s^{-4})	9(3) × 10^{-23}
Fourth derivative of pulse frequency, $\nu^{(4)}$ (s^{-5})	−3.9(8) × 10^{-28}
Fifth derivative of pulse frequency, $\nu^{(5)}$ (s^{-6})	8(1) × 10^{-34}
Sixth derivative of pulse frequency, $\nu^{(6)}$ (s^{-7})	−7.4(8) × 10^{-40}
rms timing residual (ms)	3.5
χ^2_ν/dof	1.41/45

Notes. The numbers in parentheses denote errors in the last digit. More high-order terms are required in an extensive solution to MJD 57,632 to describe the timing noise.
[a] A FWHM value in 2.3–10 keV is 0″.9 (Safi-Harb & Kumar 2008).
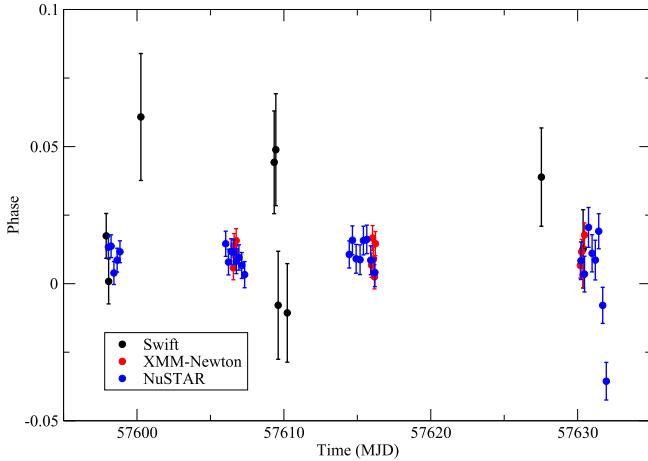
Figure 4. Residuals for the postoutburst timing solution of MJD 57,598–57,632.

but the γ-ray flux was below the detection level; therefore, we only report the flux upper limit. Even though we considered a smaller time bin (e.g., 30 days) around the outburst or included a lower energy band to investigate the γ-ray flux of PSR J1119−6127, the source flux is still significantly lower than its long-term average.

The γ-ray spectrum above 0.5 GeV from MJD 57,560–57,630 can be described by a PLEC model with a photon index of 1.5 and a cutoff energy of 3.1 GeV. The test-statistic (TS) value (Mattox et al. 1996) was only 8.4, corresponding to a confidence level less than 3σ, and it is much less significant than the detection at other epochs. If we
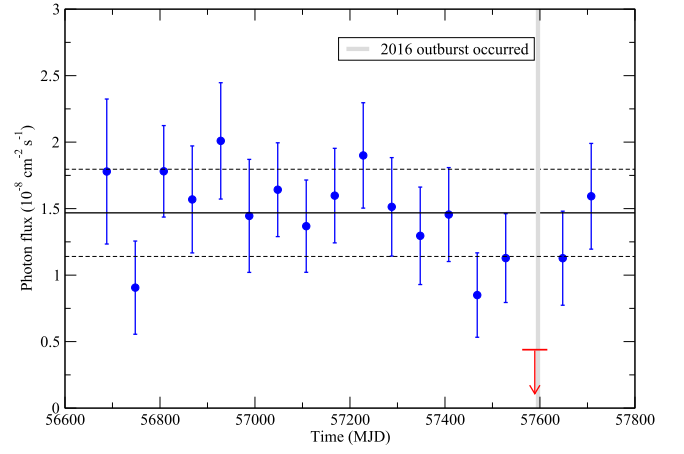
Figure 5. Variation of the γ-ray photon flux of PSR J1119−6127. Each data point represents the source flux above 500 MeV assessed from a 60 day accumulation of *Fermi* observations. The black solid and dashed lines denote the average flux and 1σ uncertainty of the pulsar, respectively. The source cannot be significantly detected by the data over MJD 57,566–57,626, and the red arrow represents the 3σ flux upper limit.

consider a longer accumulation time (i.e., MJD 56,900–57,560) in the preoutburst stage, the PLEC model has a consistent $\Gamma = 1.7 \pm 0.2$ and a cutoff energy of 3.1 ± 0.9 GeV (1σ errors). It seems that the magnetar-like outburst suppressed the γ-ray emission from the pulsar, but the major γ-ray emission mechanism did not have a significant change.

Because the postoutburst ephemeris of PSR J1119−6127 was seriously contaminated by the timing noise, it is difficult to investigate the γ-ray pulsation through a blind search. After the outburst, the effective time range of the pulsar ephemeris determined in the X-ray band (Table 2) is still too short, and the *Fermi* LAT cannot accumulate enough photons to detect the γ-ray pulsation.

3.3. Phase-averaged X-Ray Spectral Analysis

We concentrate the postoutburst spectral analysis on *XMM-Newton* and *NuSTAR* observations because *Swift* XRT and *XMM-Newton* EPIC cover a similar energy range but the effective area of *Swift*/XRT is much smaller. The spectrum obtained from each observation was rebinned with different counts (e.g., 25, 50, 75, or 100) per channel to ensure the χ^2 statistic, and the choice of the minimum was decided according to the total photons received from our target.

We fit the *XMM-Newton* and *NuSTAR* spectra jointly, since they cover a similar observational time interval. We inspected the spectral behavior of PSR J1119−6127 within 0.5–65 keV because the number of photons is insufficient beyond this energy range. We also introduced a constant in the fit to account for the cross-calibration mismatch between three EPIC cameras and two FPMs and applied a photoelectric absorption using Wisconsin cross-sections (Morrison & McCammon 1983). A single-component model did not give an acceptable result. We therefore tried the PL-plus-blackbody (BB) radiation model and double BB (2BB) model. However, except for the spectra obtained on 2016 December 12–13, the two-component models also do not provide acceptable fits. We notice that 2BB components can provide a good fit to the spectra below 10 keV, as shown in the left panel of Figure 6, and the excess in the hard X-ray band (>10 keV) can be described with an additional hard PL. Even though the PL+BB or 2BB models can provide
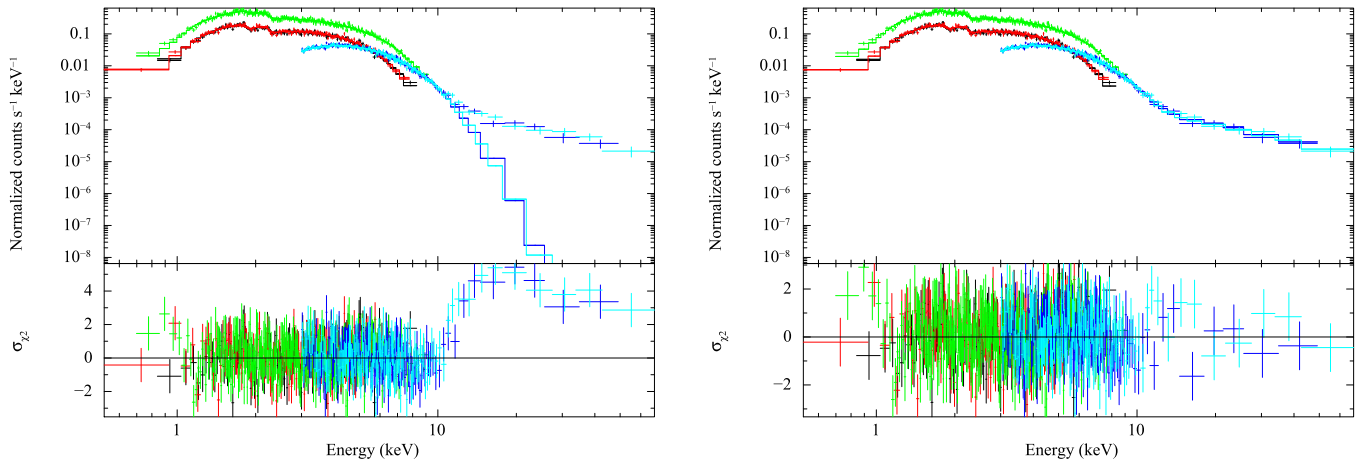
Figure 6. Joint fits to the spectra obtained from *XMM-Newton*/MOS1 (black), *XMM-Newton*/MOS2 (red), *XMM-Newton*/PN (green), *NuSTAR*/FPMA (blue), and *NuSTAR*/FPMB (cyan) on 2016 August 14–15. The left panel displays the fit to the composite model of 2BB components. The right panel presents the fit to the same model with an additional PL component (2BB+PL). The bottom panel shows the residuals in terms of χ^2.

an acceptable fit to the spectra obtained in 2016 mid-December, such an excess in the hard X-ray band is still clearly seen.

The mid-December spectra can be described by a PL+BB model ($\chi^2_\nu = 1.05$ for 283 dof) with an absorption column density (N_H) of $1.9^{+0.4}_{-0.3} \times 10^{22}$ cm^{-2}, a photon index of $3.4^{+0.8}_{-0.5}$, and an emission site of $0.16^{+0.02}_{-0.01}$ km in radius with a BB temperature of $1.18^{+0.04}_{-0.06}$ keV. All quoted errors of X-ray spectral parameters in this article correspond to a 90% confidence interval for one parameter of interest, and a source distance of 8.4 kpc was assumed (Caswell et al. 2004). The measured photon index is softer than the *Chandra* spectrum obtained in 2016 late October (Blumer et al. 2017). The unabsorbed 0.5–7 keV flux derived from our spectral model is $(3.3 \pm 1.8) \times 10^{-12}$ erg cm^{-2} s^{-1}, which is about 30%–50% lower than the nonthermal flux derived from the subsequent *Chandra* observation. The nonthermal component can be originated from the magnetospheric emission. On the other hand, we note that the soft X-ray photons (i.e., <2.5 keV) of this component contribute to a substantial fraction of the pulsed photons to lead to a large pulsed fraction ($\gtrsim 50\%$), indicating a nonthermal pulse detection. However, the pulse profiles determined in the soft and medium X-ray (i.e., 2.5–10 keV; dominated by BB component) bands have the same shape, which does not support a strong nonthermal component in the spectra.

Different from the postoutburst spectral fits to the *NuSTAR* and *Swift*/XRT data of late July, we cannot obtain an acceptable fit with the PL+BB model, except for the spectra obtained in mid-December. We tried fitting the PL+BB model to the December 12–13 spectra but obtained a totally different photon index ($3.4^{+0.8}_{-0.5}$) compared with that on July 28–29 (1.2 ± 0.2) determined in Archibald et al. (2016a). The nonthermal component in our spectra dominates the soft X-ray photons, but in the fit to the spectra of *NuSTAR* and *Swift*/XRT, it mainly describes the hard X-ray tail. Because the PL+BB model also cannot provide acceptable fits to the postoutburst spectra obtained in 2016 August, we rejected it in our investigations. Table 3 lists the best-fit parameters of the three-component model, and this model is rather common to describe the spectral behavior of magnetars (Mong & Ng 2018). Figure 6 shows the fit to the mid-August spectra, and it clearly indicates that a composite model of two thermal

and one PL component (2BB+PL) can well describe the observational features. If we only consider the *NuSTAR* spectra in 3–65 keV, the composite model with a hard PL and a single BB component can give a good fit, and it may indicate that the cooler BB component was only detected by *XMM-Newton* due to its high sensitivity at low energy.

The 2BB components determined in the 2BB+PL model can be characterized by a smaller emission site (i.e., $\lesssim 1$ km in radius) with a higher temperature of ~ 1.0 keV and a larger emission site of a few km in radius with a lower temperature of 0.3–0.4 keV. The best-fit interstellar absorption determined with the three-component model is $1.45^{+0.07}_{-0.06} \times 10^{22}$ cm^{-2}, and this value is between the postoutburst absorptions determined by Archibald et al. (2016a) and Blumer et al. (2017). Comparing with the preoutburst absorption, this value is also consistent with that from *Chandra* observations (Safi-Harb & Kumar 2008) but obviously lower than that determined by the joint fit to both *XMM-Newton* and *Chandra* spectra (Ng et al. 2012). We find that the emission sizes of two hotspots can be larger but the hotspot temperature is similar if the absorption column density is fixed at a larger value during the fit.

In addition to the BB emission, we also considered NS atmosphere models with a pure hydrogen atmosphere (NSA; Zavlin et al. 1995) and an atmosphere with hydrogen or other heavy elements (nsmax; Ho et al. 2008). PSR J1119−6127 has a strong magnetic field of $\sim 4.1 \times 10^{13}$ G; therefore, we adopted a field strength of the same order (i.e., 10^{13} G) in both the NSA and the nsmax models. Comparing with the two BB components in the three-component model, only the lower-temperature thermal component can be replaced by the emission from the magnetized atmosphere. If we considered the change of N_H at different epochs for spectral fits to the PL+NSA+BB and PL+nsmax+BB models, the best fits to both models give a consistent value of $\sim (1.4-1.6) \times 10^{22}$ cm^{-2} in August but a relatively higher value of $\sim (1.8-2.0) \times 10^{22}$ cm^{-2} in mid-December.

We did not find any obvious decreasing trend of the temperature as presented by Archibald et al. (2016a) among the spectral fits to a composite model with 2BB components shown in Table 3. We detected a trend where both hotspots shrank and their flux contribution decreased after the magnetar-like outburst. The evolution of the flux ratio between the hotter and cooler components could indicate the gradual

Table 3
Best-fit Spectral Parameters for PSR J1119−6127 Determined from *XMM-Newton* and *NuSTAR* Data

Observed Time		Aug 05–06	Aug 14–15	Aug 30–31	Dec 12–13
	$N_{\rm H}$[a]	$1.45^{+0.07}_{-0.06}$			
	Γ	0.5 ± 0.2	$0.2^{+0.3}_{-0.2}$	0.5 ± 0.2	$-0.6^{+1.2}_{-1.4}$
PL	$F_{\rm PL}$[b]	0.023	0.010	0.020	0.001
+	kT_1 (keV)	0.33 ± 0.02	$0.34^{+0.01}_{-0.02}$	0.33 ± 0.02	$0.35^{+0.02}_{-0.03}$
BB$_1$	R_1 (km)	$4.4^{+0.8}_{-0.7}$	$4.0^{+0.7}_{-0.6}$	$3.6^{+0.7}_{-0.6}$	$1.7^{+0.4}_{-0.3}$
+	$F_{\rm BB_1}$[b]	0.34	0.28	0.21	0.058
BB$_2$	kT_2 (keV)	1.03 ± 0.01	1.04 ± 0.01	1.03 ± 0.01	1.09 ± 0.04
	R_2 (km)	0.98 ± 0.02	0.81 ± 0.02	0.67 ± 0.02	0.21 ± 0.02
	$F_{\rm BB_2}$[b]	1.60	1.16	0.75	0.091
	χ^2_ν/dof	1.13/2905			
	$N_{\rm H}$[a]	1.52 ± 0.03			
PL	Γ	0.5 ± 0.2	$0.2^{+0.2}_{-0.3}$	$0.5^{+0.2}_{-0.3}$	$0.2^{+1.8}_{-1.1}$
+	$F_{\rm PL}$[b]	0.022	0.010	0.019	0.003
NSA[c]	kT_1 (eV)	234^{+4}_{-3}	224^{+4}_{-3}	210 ± 3	162^{+2}_{-6}
+	$F_{\rm NSA}$[b]	0.44	0.36	0.28	0.086
BB	kT_2 (keV)	1.03 ± 0.01	1.04 ± 0.01	1.03 ± 0.01	$1.03^{+0.03}_{-0.04}$
	R (km)	$0.97^{+0.01}_{-0.02}$	$0.81^{+0.01}_{-0.02}$	$0.67^{+0.01}_{-0.02}$	$0.24^{+0.01}_{-0.02}$
	$F_{\rm BB}$[b]	1.59	1.16	0.74	0.096
	χ^2_ν/dof	1.14/2909			
	$N_{\rm H}$[a]	$1.55^{+0.04}_{-0.02}$			
PL	Γ	$0.5^{+0.2}_{-0.3}$	$0.1^{+0.3}_{-0.2}$	$0.4^{+0.3}_{-0.2}$	$0.2^{+2.8}_{-1.2}$
+	$F_{\rm PL}$[b]	0.021	0.0095	0.018	0.0030
nsmax[d]	kT_1 (eV)	250 ± 4	240^{+4}_{-4}	224^{+4}_{-3}	172^{+3}_{-13}
+	$F_{\rm nsmax}$[b]	0.49	0.41	0.31	0.095
BB	kT_2 (keV)	1.03 ± 0.01	1.05 ± 0.01	1.03 ± 0.01	$1.04^{+0.03}_{-0.05}$
	R_2 (km)	$0.96^{+0.01}_{-0.02}$	$0.80^{+0.01}_{-0.02}$	$0.66^{+0.01}_{-0.02}$	$0.23^{+0.02}_{-0.01}$
	$F_{\rm BB_2}$[b]	1.57	1.15	0.74	0.095
	χ^2_ν/dof	1.14/2909			

Notes. The evolution of each parameter in the PL+2BB model is shown in Figure 8.
[a] The linked absorption column density is in units of 10^{22} cm^{-2}.
[b] The unabsorbed flux is measured in 0.5–10 keV and recorded in units of 10^{-11} erg cm^{-2} s^{-1}.
[c] We assumed an NS mass of 1.4 $M_\odot$, a radius of 13 km, and a magnetic field of 10^{13} G.
[d] We use 1.4 $M_\odot$ in mass and 10 km of radius in size to derive the gravitational redshift. The model number is fixed as 1300 for magnetar-like pulsars. The emitting size is the same as described in Footnote c).

disappearance of the hotter spot. The decrease of the temperature can be detected if we replace the cooler thermal component by the global atmospheric emission with a uniform temperature.

3.4. Phase-resolved X-Ray Spectral Analysis

Based on the result of the phase-averaged spectral analysis shown in Table 3, we find that the two thermal components dominate the spectral behavior in the energy range $\lesssim 10$ keV. The background-subtracted pulsed fractions can be determined by $(f_{\rm max} - f_{\rm min})/(f_{\rm max} + f_{\rm min})$, where $f_{\rm max}$ and $f_{\rm min}$ are the maximum and minimum counts in the folded bins, respectively. These values inferred from four *XMM-Newton*/PN data are 66% ± 2%, 70% ± 2%, 67% ± 3%, and 87% ± 5%, while the *NuSTAR* observations give 65% ± 2%, 61% ± 2%, 49% ± 3%, and 74% ± 11% at similar epochs. The pulsed fraction obtained from the *XMM-Newton*/PN observations is higher, and no pulsation can be detected >10 keV after end of July; thus, we speculate that the additional PL component required in the joint spectral analysis with *NuSTAR* observations has no contribution to the pulsations of PSR J1119−6127. Accordingly, we only

generated the pulsed spectra of different epochs from the *XMM-Newton*/PN observations.

As shown in Figure 7, we defined the phase intervals of 0.46–0.92, 0.88–1.38, 0.12–0.60, and 0.56–0.98 as the "on-pulse" components for data observed on 2016 August 6, 15, and 30 and December 13, respectively. The "off-pulse" (i.e., DC level) interval in the folded light curve was then determined at the phase within 0.96–1.38, 0.44–0.84, 0.64–1.06, and 0.06–0.48 for data observed on 2016 August 6, 15, and 30 and December 13, respectively. We generated pulsed spectra at different epochs by subtracting the "off-pulse" spectra from the "on-pulse" spectra. In order to ensure the χ^2 statistic, we regrouped the channels to have at least 50, 80, 50, and 25 photons per channel for each observation gained from 2016 early August to mid-December We also generated the unpulsed spectra by subtracting the background contribution from the source spectrum gained within the "off-pulse" interval as defined in Figure 7, and the background spectrum was determined by the nearby source-free region. The unpulsed spectrum was also rebinned with a minimum of 25, 40, 25, and 15 counts per channel for each data set observed from 2016 early August to mid-December.
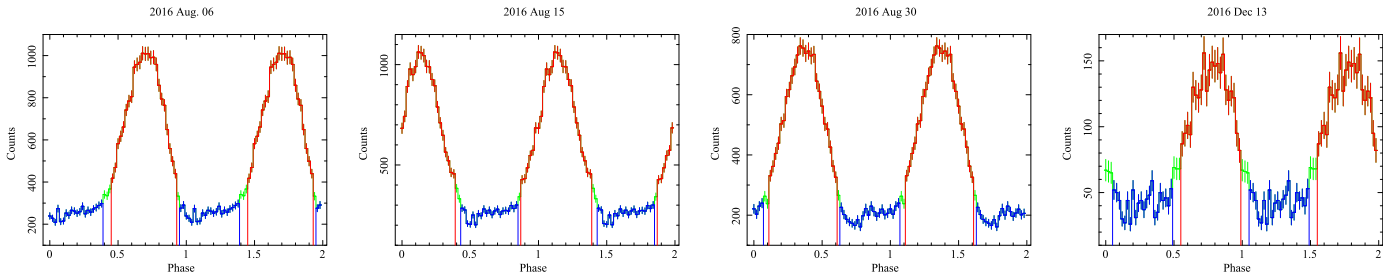
Figure 7. Folded light curves of PSR J1119−6127 in 0.15–12 keV obtained from four *XMM-Newton*/PN observations. It is a folded light curve at MJDs 57,606.6, 57,616.0, 57,630.3, and 57,735.5 with spin frequencies of 2.4398214, 2.4397945, 2.4397218, and 2.4391766 Hz, respectively. The regions under the red and blue curves represent the on- and off-pulse phases, respectively, in each profile. Two cycles of each profile are shown for clarity.

3.4.1. Pulsed Spectral Analysis

A single PL or BB model does not provide a good fit to most of the individual pulsed spectrum. Although the PL+BB model can provide acceptable fits to the pulsed spectra, the photon index is abnormally large (i.e., >2.5) compared to the general nonthermal X-ray emission from pulsars (Cheng & Zhang 1999). In addition, the nonthermal component dominates both the source flux and the spectra in the soft X-ray band. We infer that the dominant nonthermal component also contributes to the pulsed emission, since it was obtained from the pulsed spectra. The nonthermal pulsations corresponding to a different physical origin should have a more distinct profile than the thermal pulsation originated from the surface emission. For example, the synchrotron radiation in the magnetosphere has a pulse profile similar to what we detected in the hard X-ray band with *NuSTAR* (Figure 2), and it is different from the profile obtained from the BB component. Nevertheless, we obtain similar structure without any phase change in the energy-resolved pulse profiles below 10 keV, and it disfavors the existence of different physical origins in the pulsed spectra.

We present the simultaneous fit to the pulsed spectrum with 2BB components and a linked hydrogen absorption in Table 4. The thermal flux derived for the two hotspots and the inferred emission size are somewhat lower/smaller than what we obtain in Table 3 but are still statistically consistent. Because the composite model contributed by two thermal components provides a better fit and a more physical origin, this is our preferred model. We cannot conclude that a significant change in the temperature of each thermal component derived from different observations, but the shrinking of both emitting regions led to a decreasing pulsed emission with time.

3.4.2. Unpulsed Spectral Analysis

The unpulsed spectra of PSR J1119−6127 extracted from the "off-pulse" phase can be adequately fit by a single BB model, and the results are listed in Table 5, in contrast to the phase-averaged and pulsed spectra. However, the fit prefers a small N_H, lower than all previously reported values (e.g., $(1.1 \pm 0.1) \times 10^{22}$ cm^{-2}; Blumer et al. 2017). Adding another BB component gives a larger absorption (see Table 5). If we fix N_H at a higher value, we obtain lower temperatures for the BB components, e.g., $N_H = 1.6 \times 10^{22}$ cm^{-2} gives $kT = 0.43^{+0.06}_{-0.07}$ and $1.18^{+0.07}_{-0.06}$ eV for the 2016 August 6 data. The thermal component at the off-pulse phase has a similar temperate but a smaller effective radius (13%–70% for the cooler component and 16%–60% for the hotter component) than that at the on-pulse phase. Hence, we speculate that only part of the thermal emission can be observed at the off-pulse phase through a

light-bending effect due to the strong gravity, even though the hotspot is not in the line of sight.

The BB+PL model can also provide acceptable fits to the spectra. However, NSA+PL does not provide a good fit to the spectrum. The best-fit PL+BB model has $N_H = (1.7 \pm 0.3) \times 10^{22}$ cm^{-2} and a large photon index ($\Gamma \gtrsim 3$). Such a large absorption was also obtained in the preoutburst spectral analysis of PSR J1119−6127. The unabsorbed flux contributed by the thermal and nonthermal components is comparable. We note that this PL component could not be contributed from PWNe because such a large photon index was rarely obtained by the nonthermal X-rays from PWNe (Kargaltsev & Pavlov 2008). However, the soft nonthermal component could be originated from the magnetospheric upscattering of the thermal photons (Thompson et al. 2002).

4. Discussion

The positive detections of X-ray pulsations for PSR J1119−6127 after 2016 early September are few, and we cannot extend the effective time range of the ephemeris (see Table 2) through the TOA analysis. According to the spin-down rate derived by the linear regression over different time ranges, our results did not show any hints of its recovery. Instead of the spin-down recovery that can be observed after two previous glitches (Weltevrede et al. 2011; Antonopoulou et al. 2015) or after the glitch event of other high-B pulsars (Livingstone et al. 2011), we suspect that some events occurring at the end of 2016 August could have slowed down the pulsar spin and continuously increased its spin-down rate. Three short magnetar-like X-ray bursts detected on 2016 August 30 may relate to not only the change of the radio pulse profile (Archibald et al. 2017) but also the increase of the timing noise and spin-down rate.

Dai et al. (2018) observed the pulsar regularly with the Parkes radio telescope and presented a complete evolution of the timing solution. According to their results, both the radio flux and the spin-down rate of the pulsar continued to increase after the outburst at the end of July until the end of August. The complicated timing behavior well followed the expectation of our timing analysis, although we do not have enough dense data sets to trace the recovery of the spin-down rate starting from the end of August. During the recovery process, a two-component radio pulse profile transformed into a four-component one accompanying a sudden flux drop in the radio band.

We need two thermal components to fit the X-ray spectra in our spectral analysis. An NS with a strong toroidal magnetic field can lead to the discontinuities in the tangential B-field component, where the ohmic dissipation is strongly enhanced

Table 4
Best-fit Parameters for the Pulsed Spectra of PSR J1119−6127 Obtained from *XMM-Newton*/PN

Observed Time		Aug 06	Aug 15	Aug 30	Dec 13
	N_{H}[a]	0.85 ± 0.04			
BB	kT (keV)	1.01 ± 0.02	0.96 ± 0.02	$0.93^{+0.02}_{-0.03}$	0.79 ± 0.05
	R (km)	1.01 ± 0.04	$0.90^{+0.04}_{-0.03}$	$0.78^{+0.03}_{-0.04}$	0.40 ± 0.04
	F_{BB}[b]	1.52	1.02	0.66	0.093
	χ^2_ν/dof	1.25/569			
	N_{H}[a]	1.8 ± 0.2			
PL	Γ	$3.2^{+0.7}_{-0.5}$	3.0 ± 0.5	$2.7^{+0.6}_{-0.4}$	$3.2^{+0.7}_{-0.6}$
+	F_{PL}[b]	1.58	1.19	0.93	0.27
BB	kT (keV)	1.00 ± 0.03	$0.97^{+0.03}_{-0.04}$	$0.96^{+0.07}_{-0.09}$	$1.2^{+0.2}_{-0.2}$
	R (km)	$0.99^{+0.09}_{-0.08}$	$0.81^{+0.07}_{-0.08}$	$0.58^{+0.1}_{-0.09}$	$0.13^{+0.06}_{-0.07}$
	F_{BB}[b]	1.42	0.84	0.41	0.044
	χ^2_ν/dof	1.10/561			
	N_{H}[a]	$1.3^{+0.1}_{-0.2}$			
	kT_1 (keV)	$0.37^{+0.12}_{-0.07}$	$0.45^{+0.10}_{-0.08}$	$0.46^{+0.11}_{-0.08}$	$0.38^{+0.06}_{-0.05}$
BB$_1$	R_1 (km)	3^{+2}_{-1}	$2.1^{+1.0}_{-0.7}$	$1.9^{+0.8}_{-0.6}$	$1.4^{+0.6}_{-0.4}$
+	$F_{\mathrm{BB_1}}$[b]	0.24	0.25	0.24	0.060
BB$_2$	kT_2 (keV)	$1.01^{+0.05}_{-0.03}$	$1.03^{+0.06}_{-0.05}$	$1.08^{+0.11}_{-0.08}$	$1.2^{+0.1}_{-0.2}$
	R_2 (km)	$1.00^{+0.08}_{-0.10}$	$0.76^{+0.09}_{-0.11}$	0.5 ± 0.1	0.17 ± 0.05
	$F_{\mathrm{BB_2}}$[b]	1.53	0.94	0.55	0.071
	χ^2_ν/dof	1.07/561			

Notes.
[a] The linked absorption column density is in units of 10^{22} cm^{-2}.
[b] The unabsorbed flux is measured in 0.5–8 keV and recorded in units of 10^{-11} erg cm^{-2} s^{-1}.

(Viganò & Pons 2012), affecting the thermal evolution through Joule heating. The heat conduction then becomes anisotropic, resulting in inhomogeneous surface temperature distributions (Viganò et al. 2013). The thermal pulse profile can eventually evolve into single-peaked with a large pulsed fraction (Perna et al. 2013); however, PSR J1119−6127 is a young pulsar with a characteristic age of only 1600 yr. The cooler surface emission can be hidden under the case of strong interstellar absorption ($N_{\mathrm{H}} \gtrsim 10^{22}$ cm^{-2}), and the detected thermal component of the NS within the energy band of 0.5–2 keV only reveals a single hotspot of about 1–2 km (cf. simulations in Shabaltas & Lai 2012). Nevertheless, the cooler hotspot obtained in our X-ray spectral fit has a temperature of >0.3 keV and contributes to a significant fraction of photons below 2.5 keV, so a more complete model to reinvestigate how the multiple thermal components lead to a single-peaked profile is required. The contribution of a cooler but larger thermal component can also be described by the global magnetized atmospheric emission with a uniform temperature. Because the cooler thermal emission also has a substantial contribution to the pulsations, we speculate that the emission scenario from two local hotspots could explain the observed pulsed structure. We also note that the hotter thermal emission in the composite model can be replaced by a Comptonization component (i.e., CompBB model; Nishimura et al. 1986), and the BB temperature of the Comptonized model is consistent with that determined for the surface emission.

We cannot differentiate the contribution of the nonthermal component dominated in the soft X-ray pulsation (i.e., <2.5 keV) from the thermal pulsation, although the BB+PL model can also provide an acceptable fit to the phase-averaged spectra below 10 keV. Comparing with the flux of PWNe detected in the postoutburst stage (Blumer et al. 2017) and the time required to

power it by the 2016 bursts, the unabsorbed flux contribution larger than 10^{-12} erg cm^{-2} s^{-1} with a steep photon index of $\Gamma \gtrsim 3$ should result from the different origin, even if we cannot exclude a negligible contribution from the PWN. The similar combined components can also be resolved in the pulsed spectra extracted from the *XMM-Newton* observations, as shown in Table 4. However, a nonthermal origin to emit a large amount of soft X-ray photons is not preferred to describe the pulsed emission because we did not find a pulsed structure change comparing with the thermal origin. An additional PL component with $\Gamma < 1$ is indeed required to describe the spectral behavior in the hard X-ray band (i.e., >10 keV) when we further include the spectra obtained by *NuSTAR* observations. Because the soft photon index (2.2 ± 0.5) determined by the spectrum of PWN in the postoutburst stage (Blumer et al. 2017) is much softer, we argue that this component should be attributed to the magnetospheric emission of PSR J1119−6127. This component cannot result from the outer gap emission of the pulsar after the end of 2016 July because we detected more than 2000 source counts over 10 keV but the pulsations were not significant at all. Such a hard component was also detected in some persistently bright magnetars (e.g., 4U 0142+61) or from the spectral slope changes of some transient magnetars (e.g., 1E 1547.0−5408) during outbursts (Enoto et al. 2017).

Both the phase-averaged and pulsed spectral analyses did not show an obvious temperature variation for the two thermal components, but we can detect a trend of decreasing emission area, as shown in Figure 8. A similar feature was also observed in the outburst decay of some magnetars (Esposito et al. 2013; Rodríguez Castillo et al. 2016). The decrease in temperature can only be seen when the cooler BB component with a temperature of 0.3–0.4 keV is replaced by the NS atmosphere model. When we perform a simultaneous fit to the pulsed spectrum with a
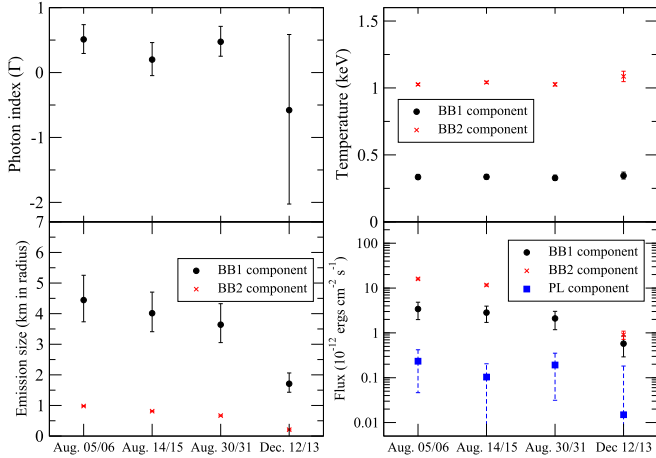
Table 5
Best-fit Parameters for the Unpulsed Spectra of PSR J1119−6127 Obtained from *XMM-Newton*/PN

Observed Time		Aug 06	Aug 15	Aug 30	Dec 13
BB	N_H[a]	$0.79^{+0.04}_{-0.05}$			
	kT (keV)	$1.09^{+0.03}_{-0.02}$	1.11 ± 0.02	1.11 ± 0.03	1.1 ± 0.1
	R (km)	$0.61^{+0.02}_{-0.03}$	0.51 ± 0.02	0.41 ± 0.02	0.12 ± 0.02
	F_{BB}[b]	0.74	0.55	0.36	0.033
	χ^2_ν/dof	1.09/488			
PL	N_H[a]	1.7 ± 0.3			
+	Γ	2.2 ± 0.5	$3.0^{+0.8}_{-0.7}$	2.9 ± 0.8	3^{+5}_{-2}
BB	F_{PL}[b]	0.66	0.46	0.28	0.035
	kT (keV)	$1.05^{+0.09}_{-0.10}$	$1.13^{+0.04}_{-0.03}$	$1.12^{+0.04}_{-0.05}$	1.2 ± 0.5
	R (km)	$0.53^{+0.10}_{-0.08}$	0.46 ± 0.05	0.38 ± 0.04	$0.09^{+0.06}_{-0.07}$
	F_{BB}[b]	0.48	0.49	0.31	0.023
	χ^2_ν/dof	1.01/480			
BB$_1$	N_H[a]	1.2 ± 0.2			
+	kT_1 (keV)	$0.6^{+0.2}_{-0.1}$	$0.37^{+0.11}_{-0.09}$	$0.40^{+0.15}_{-0.09}$	$0.4^{+0.6}_{-0.2}$
BB$_2$	R_1 (km)	$1.2^{+0.6}_{-0.4}$	$1.8^{+1.4}_{-0.8}$	$1.2^{+0.5}_{-1.0}$	$0.5^{+2.3}_{-0.4}$
	F_{BB_1}[b]	0.25	0.083	0.053	0.0082
	kT_2 (keV)	$1.3^{+0.3}_{-0.1}$	$1.14^{+0.05}_{-0.04}$	$1.14^{+0.06}_{-0.05}$	$1.23^{+0.04}_{-0.18}$
	R_2 (km)	$0.4^{+0.1}_{-0.2}$	$0.48^{+0.04}_{-0.05}$	$0.39^{+0.03}_{-0.05}$	$0.10^{+0.04}_{-0.10}$
	F_{BB_2}[b]	0.58	0.54	0.35	0.031
	χ^2_ν/dof	1.00/480			

Notes. The evolution of each parameter in the PL+BB and 2BB models can be referred to Figures 9 and 10.
[a] The linked absorption column density is in units of 10^{22} cm^{-2}.
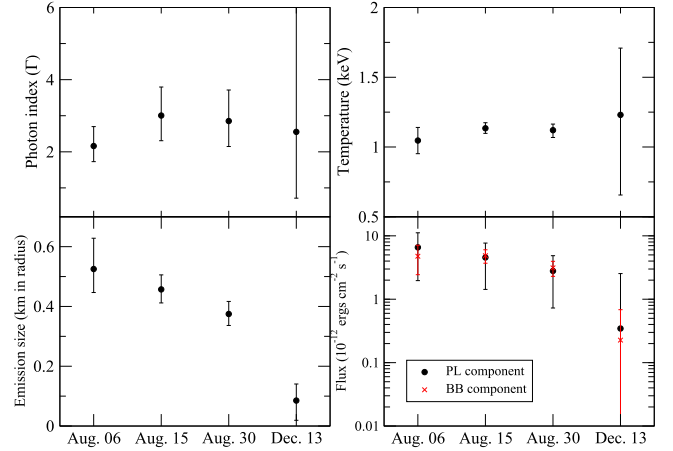[b] The unabsorbed flux is measured in 0.5–8 keV and recorded in units of 10^{-11} erg cm^{-2} s^{-1}.

Figure 8. Spectral parameters obtained by the simultaneous fit to the joint spectra of *XMM-Newton* and *NuSTAR* observations with the PL+2BB model and a linked absorption. The parameters are listed in Table 3. The error bars denote 90% confidence intervals.
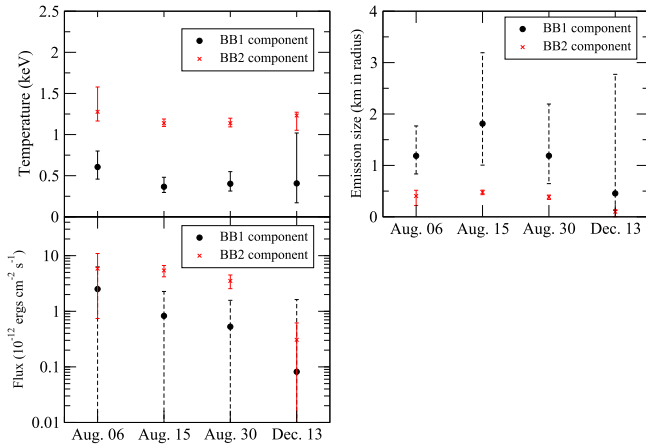

Figure 9. Spectral parameters obtained by the simultaneous fit to the unpulsed spectra with PL+BB model components and a linked absorption. The parameters are listed in Table 5. The error bars denote 90% confidence intervals.

linked absorption ($N_H = 1.59^{+0.07}_{-0.09} \times 10^{22}$ cm^{-2}) with the NSA+BB model, we find a uniform temperature over the entire surface of a 1.4 $M_\odot$ NS with 13 km radius evolved with 245^{+13}_{-9}, 234^{+9}_{-10}, 223^{+8}_{-9}, and 172^{+5}_{-6} eV obtained from the *XMM-Newton* data on August 06, August 15, August 30, and December 13, respectively.

In the unpulsed spectral analysis, both of the composite models, PL+BB and 2BB, provide acceptable fits with the spectral parameters shown in Figures 9 and 10. The resonant cyclotron scattering of the surface thermal emission (Thompson et al. 2002) and the gravitational bending of the emission from

the warmer hotspot may provide the radiative scenario of the PL+BB model. The nonthermal emission, which dominates the soft X-ray photons (i.e., <2.5 keV), is comparable to the surface emission in this model; nevertheless, the effect of resonant Compton scattering mainly produces the hard X-ray photons, and it is difficult to explain the off-pulse emission with such a soft PL component. It is also strange that both the pulsed and off-pulsed emission have similar emission origins, but we note that the emission sizes of two hotspots determined by the unpulsed spectra (i.e., from 1.8 to 0.5 km for the larger hotspot radius and from 0.48 to 0.10 km for the smaller one)

Figure 10. Spectral parameters obtained by the simultaneous fit to the unpulsed spectra with 2BB components and a linked absorption. The parameters are listed in Table 5. The error bars denote 90% confidence intervals.

are smaller that those inferred from the fit to the pulsed spectrum (i.e., from 3.0 to 1.4 km for the larger hotspot radius and from 1.00 to 0.17 km for the smaller one). This result suggests that the emission from hotspots, which is not in the direction of our sight, can still be partially observed due to the gravitational light bending and contributes weaker thermal components in the spectra during the off-pulse phase.

Around the X-ray outburst of PSR J1119−6127, we found the source flux $F_{0.5-300\,\mathrm{GeV}} < 4.9 \times 10^{-12}$ erg cm^{-2} s^{-1}, which is clearly lower than the $(1.2 \pm 0.1) \times 10^{-11}$ erg cm^{-2} s^{-1} determined in the preoutburst stage. Although the significance of the detection was clearly decreased, similar γ-ray spectral behavior can be inspected before and during the outburst stages. It indicates that the acceleration mechanism to emit γ-ray photons was suppressed without a significant change in the emission geometry. The theoretical model for the evolution of the γ-ray and X-ray emission after the outburst will be fully discussed in our subsequent paper. Similar suppression after the outburst can also be detected in the radio band at the end of 2016 July or early August (Majid et al. 2017).

It is not clearly understood what caused the increase of the spin-down rate with a month timescale and the disappearance of the radio emission after the glitch, but it could be related to a reconfiguration of the open field line region (Parfrey et al. 2012; Akbal et al. 2015; Huang et al. 2016). Changes of the global magnetospheric configuration are also expected for some transient RPPs, for which two emitting states with different spin-down states have been observed. For example, PSR B1931+24 transferred between radio-bright and radio-quiet modes with a timescale from days to weeks (Kramer et al. 2006). PSR J2021+4026 showed a mode change in γ-rays during a glitch in 2011 and stayed at a low γ-ray luminosity with high spin-down rate for about 3 yr (Zhao et al. 2017). Moreover, PSR B0943+10 showed synchronous mode-switching between the radio and the X-ray emission (Hermsen et al. 2013; Mereghetti et al. 2016). We note that a similar synchronous change can be detected for PSR J1119 −6127 after the 2016 outburst. The X-ray background-subtracted pulsed fractions of PSR J1119−6127 obtained from *NuSTAR* on July 28–29 and August 30–31 are 63% ± 2% and 49% ± 3%, which could also indicate a relatively higher ratio of nonthermal contribution when the radio emission was

switched on. Although the physical origin of our detections can be different from that of RPPs, and the mode change of the latter could be a state change of the global magnetospheric current, triggers of the state changes in the electromagnetic emission and/or the spin-down rate are not yet well understood and could depend on the type of transients.

It is difficult to evaluate the effect on the timing solution due to the short magnetar-like bursts occurring at the end of 2016 August in our study, so we cannot definitively conclude that the larger spin-down rate was caused by the reconfiguration of the global magnetosphere. Another interpretation is that a large number of electron–positron pairs created in the trapped photon-pair plasma fireball cease the entire acceleration mechanism of an NS (Thompson & Duncan 1995). Such a scenario was also applied to explain the sudden radio drop over a few tens of s coincident with the occurrence of multiple short X-ray bursts detected at the end of 2016 August (Archibald et al. 2017). The series of X-ray bursts occurring at the end of 2016 July can also provide the energy of the trapped fireball to create the pairs to suppress the radio and high-energy emission. The major difference after the X-ray bursts at the end of July and August may be the cooling timescale of the pair plasma in the trapped fireball because no significant radio detection was obtained until 2016 August 1 (Majid et al. 2017), and it seems that the recovery of the radio emission required a longer time.

5. Conclusion

We have performed a complete study to trace the high-energy timing and spectral evolution of PSR J1119−6127 after its 2016 outburst. Based on the confirmed periodic signals detected at different epochs, we derived the timing ephemeris of PSR J1119−6127 after the outburst. We also clearly found the decreasing trend of the spin frequency derivative after the glitch/outburst, which is different from the recovery of the spin-down rate generally observed following similar events or even in the previous glitches of 2004 and 2007. The serious timing noise embedded in the timing solution can be detected at the end of 2016 August by comparing ephemerides determined within different time intervals in Table 2, and it also prohibits blind searches of pulsations in γ-rays.

In the beginning of the 2016 outburst, the X-ray emission of <10 keV in the phase-averaged spectroscopy can be mainly described with a single thermal component. After the outburst, we found that the spectrum requires two thermal components to describe X-rays from different origins: the global atmosphere/large emitting region (with a few km in radius) and the small hotspot (with a radius less than 1 km). Comparing with the spectral behavior of the pulsar before the 2016 outburst, the pulsed fraction in 2.5–8 keV significantly increased, and an additional component is required to fit the spectrum. Instead of a decrease in the temperature after the outburst, we found that the emission sites shrank to ∼65% and 80% of their original size in 4 months. A shrinking of the thermal emitting region is also detected to be accompanied by a decrease of the flux. The decrease of the temperature is only significant when we replace the cooler thermal component of ∼0.3–0.4 keV with the magnetized atmospheric emission, but we did not prefer such an interpretation because the pulsed emission in the soft X-ray band (<2.5 keV) was quite significant, inconsistent with a global emission scenario. We also need to include a hard PL component ($\Gamma < 1$) to describe the hard X-ray (>10 keV)

spectrum from *NuSTAR*. Such a component with an unclear origin cannot be detected in RPPs in general; even another high-*B* pulsar, PSR J1846−0258, shows an obvious softening of the nonthermal emission in the outburst (Ng et al. 2008). Comparing with strong thermal emission from the pulsar, the emission from the PWN and magnetospheric pulsation is low and cannot be clearly resolved from the spectra after the outburst.

The γ-ray flux of PSR J1119−6127 obviously decreased when the outburst occurred in 2016, but the spectral parameters are similar to those determined in the preoutburst state. The suppression of the radio emission was also detected at the outburst, and similar transitions of the radio flux for a pulsar were also in the mode-changing RPPs. Based on our studies, we find that after the outburst, the emission from the magnetosphere had a higher flux ratio ($\sim$30%) between the nonthermal and total flux of 3–65 keV if the contribution from the PWN did not have a significant change between epochs. Such a high flux ratio contributed by the magnetospheric emission is also found to accompany the active radio emission state. We also note that the pulsar had the largest spin-down rate between the end of 2016 August and early September when the radio emission of the pulsar was brightest (Dai et al. 2018). Additional support for this picture in our analysis is that the magnitude of the frequency derivative reported by Archibald et al. (2016a) is much smaller than the value we found before 2016 early September, while the radio pulsar was still active.

Facilities: *Fermi*(LAT), *Swift*(XRT), *XMM*(EPIC), *NuSTAR*.

Software: xspec (Dorman & Arnaud 2001), heasoft (https://heasarc.nasa.gov/lheasoft/), Fermi Science Tools (https://fermi.gsfc.nasa.gov/ssc/data/analysis/documentation/), XMM–Newton SAS (https://www.cosmos.esa.int/web/xmm-newton/sas-news).

ORCID iDs

Lupin Chun-Che Lin ⓘ https://orcid.org/0000-0003-4083-9567
Jumpei Takata ⓘ https://orcid.org/0000-0002-8731-0129
Chin-Ping Hu ⓘ https://orcid.org/0000-0001-8551-2002
C.-Y. Ng ⓘ https://orcid.org/0000-0002-5847-2612
C. Y. Hui ⓘ https://orcid.org/0000-0003-1753-1660
A. K. H. Kong ⓘ https://orcid.org/0000-0002-5105-344X
Pak-Hin T. Tam ⓘ https://orcid.org/0000-0002-1262-7375

References

Acero, F., Ackermann, M., Ajello, M., et al. 2015, ApJS, 218, 23
Akbal, O., Gü gercinoğlu, E., Şaşmaz Muş, S., & Alpar, M. A. 2015, MNRAS, 449, 933
Antonopoulou, D., Vasilopoulos, G., & Espinoza, C. M. 2016, ATel, 9282, 1
Antonopoulou, D., Weltevrede, P., Espinoza, C. M., et al. 2015, MNRAS, 447, 3924
Archibald, A. M., Kaspi, V. M., Livingstone, M. A., & McLaughlin, M. A. 2008, ApJ, 688, 550
Archibald, R. F., Burgay, M., Lyutikov, M., et al. 2017, ApJL, 849, L20
Archibald, R. F., Kaspi, V. M., Tendulkar, S. P., & Scholz, P. 2016a, ApJL, 829, L21
Archibald, R. F., Kaspi, V. M., Tendulkar, S. P., & Scholz, P. 2018, ApJ, submitted (arXiv:1806.01414)
Archibald, R. F., Tendulkar, S. P., Scholz, P. A., & Kaspi, V. M. 2016b, ATel, 9284, 1
Blumer, H., Safi-Harb, S., & McLaughlin, M. A. 2017, ApJL, 850, L18
Burgay, M., Israel, G. L., Possenti, A., et al. 2009, ATel, 1913, 1
Camilo, F., Kaspi, V. M., Lyne, A. G., et al. 2000, ApJ, 541, 367
Camilo, F., Ransom, S. M., Halpern, J. P., et al. 2006, Natur, 442, 892
Caswell, J. L., McClure-Griffiths, N. M., & Cheung, M. C. M. 2004, MNRAS, 352, 1405
Cheng, K. S., & Zhang, L. 1999, ApJ, 515, 337
Dai, S., Johnston, S., Weltevrede, P., et al. 2018, MNRAS, 480, 3584
de Jager, O. C., & Büsching, I. 2010, A&A, 517, L9
Dib, R., Kaspi, V. M., & Gavriil, F. P. 2008, ApJ, 673, 1044
Dorman, B., & Arnaud, K. A. 2001, in ASP Conf. Ser. 238, Astronomical Data Analysis Software and Systems X, ed. F. R. Harnden, Jr, F. A. Primini, & H. E. Payne (San Francisco, CA: ASP), 415
Enoto, T., Shibata, S., Kitaguchi, T., et al. 2017, ApJS, 231, 8
Esposito, P., Tiengo, A., Rea, N., et al. 2013, MNRAS, 429, 3123
Gavriil, F. P., Gonzalez, M. E., Gotthelf, E. V., et al. 2008, Sci, 319, 1802
Gibson, A. I., Harrison, A. B., Kirkman, I. W., et al. 1982, Natur, 296, 833
Göğüş, E., Lin, L., Kaneko, Y., et al. 2016, ApJL, 829, L25
Gonzalez, M., & Safi-Harb, S. 2003, ApJL, 591, L143
Gonzalez, M. E., Kaspi, V. M., Camilo, F., Gaensler, B. M., & Pivovaroff, M. J. 2005, ApJ, 630, 489
Harrison, F. A., Craig, W. W., Christensen, F. E., et al. 2013, ApJ, 770, 103
Hermsen, W., Hessels, J. W. T., Kuiper, L., et al. 2013, Sci, 339, 436
Ho, W. C. G., Potekhin, A. Y., & Chabrier, G. 2008, ApJS, 178, 102
Hobbs, G., Faulkner, A., Stairs, I. H., et al. 2004, MNRAS, 352, 1439
Hu, C.-P., Ng, C.-Y., Takata, J., Shannon, R. M., & Johnston, S. 2017, ApJ, 838, 156
Huang, L., Yu, C., & Tong, H. 2016, ApJ, 827, 80
Kargaltsev, O., & Pavlov, G. G. 2008, in AIP Conf. Ser. 983, 40 Years of Pulsars: Millisecond Pulsars, Magnetars and More, ed. C. Bassa et al. (Melville, NY: AIP), 171
Kaspi, V. M., & Beloborodov, A. M. 2017, ARA&A, 55, 261
Kaspi, V. M., & McLaughlin, M. A. 2005, ApJL, 618, L41
Kennea, J. A., Lien, A. Y., Marshall, F. E., et al. 2016, GCN Circular Service, 1, 19735
Kramer, M., Lyne, A. G., O'Brien, J. T., Jordan, C. A., & Lorimer, D. R. 2006, Sci, 312, 549
Leahy, D. A. 1987, A&A, 180, 275
Livingstone, M. A., Ng, C.-Y., Kaspi, V. M., Gavriil, F. P., & Gotthelf, E. V. 2011, ApJ, 730, 66
Livingstone, M. A., Ransom, S. M., Camilo, F., et al. 2009, ApJ, 706, 1163
Majid, W., Dobreva, T., Kocz, J., et al. 2016, ATel, 9321, 1
Majid, W. A., Pearlman, A. B., Dobreva, T., et al. 2017, ApJL, 834, L2
Mardia, K. 1972, Statistics of Directional Data (New York: Academic)
Mattox, J. R., Bertsch, D. L., Chiang, J., et al. 1996, ApJ, 461, 396
McLaughlin, M. A., Stairs, I. H., Kaspi, V. M., et al. 2003, ApJL, 591, L135
Mereghetti, S., Kuiper, L., Tiengo, A., et al. 2016, ApJ, 831, 21
Mong, Y.-L., & Ng, C.-Y. 2018, ApJ, 852, 86
Morrison, R., & McCammon, D. 1983, ApJ, 270, 119
Ng, C.-Y., & Kaspi, V. M. 2011, in AIP Conf. Proc. 1379, Astrophysics of Neutron Stars 2010: A Conference in Honor of M. Ali Alpar, ed. E. Göğüş, T. Belloni, & Ü. Ertan (AIP: Melville, NY), 60
Ng, C.-Y., Kaspi, V. M., Dib, R., et al. 2011, ApJ, 729, 131
Ng, C.-Y., Kaspi, V. M., Ho, W. C. G., et al. 2012, ApJ, 761, 65
Ng, C.-Y., Slane, P. O., Gaensler, B. M., & Hughes, J. P. 2008, ApJ, 686, 508
Nishimura, J., Mitsuda, K., & Itoh, M. 1986, PASJ, 38, 819
Parent, D., Kerr, M., den Hartog, P. R., et al. 2011, ApJ, 743, 170
Parfrey, K., Beloborodov, A. M., & Hui, L. 2012, ApJL, 754, L12

Perna, R., & Pons, J. A. 2011, ApJL, 727, L51

Perna, R., Viganò, D., Pons, J. A., & Rea, N. 2013, MNRAS, 434, 2362

Pivovaroff, M. J., Kaspi, V. M., Camilo, F., Gaensler, B. M., & Crawford, F. 2001, ApJ, 554, 161

Pons, J. A., & Geppert, U. 2007, A&A, 470, 303

Pons, J. A., & Rea, N. 2012, ApJL, 750, L6

Ray, P. S., Kerr, M., Parent, D., et al. 2011, ApJS, 194, 17

Rea, N., Israel, G. L., Pons, J. A., et al. 2013, ApJ, 770, 65

Rodríguez Castillo, G. A., Israel, G. L., Tiengo, A., et al. 2016, MNRAS, 456, 4145

Safi-Harb, S., & Kumar, H. S. 2008, ApJ, 684, 532

Shabaltas, N., & Lai, D. 2012, ApJ, 748, 148

Thompson, C. 2008, ApJ, 688, 499

Thompson, C., & Duncan, R. C. 1995, MNRAS, 275, 255

Thompson, C., & Duncan, R. C. 1996, ApJ, 473, 322

Thompson, C., Lyutikov, M., & Kulkarni, S. R. 2002, ApJ, 574, 332

Viganò, D., & Pons, J. A. 2012, MNRAS, 425, 2487

Viganò, D., Rea, N., Pons, J. A., et al. 2013, MNRAS, 434, 123

Weltevrede, P., Johnston, S., & Espinoza, C. M. 2011, MNRAS, 411, 1917

Woods, P. M., & Thompson, C. 2006, in Soft Gamma Repeaters and Anomalous X-ray Pulsars: Magnetar Candidates, ed. W. H. G. Lewin & M. van der Klis (Cambridge: Cambridge Univ. Press), 547

Younes, G., Kouveliotou, C., & Roberts, O. 2016, GCN, Circular Service, 1, 19736

Zavlin, V. E., Pavlov, G. G., Shibanov, Y. A., & Ventura, J. 1995, A&A, 297, 441

Zhao, J., Ng, C. W., Lin, L. C. C., et al. 2017, ApJ, 842, 53